

1        **Link between crustal thickness and Moho transition zone at 9°N East Pacific Rise**

2                                Zhikai Wang<sup>1,2</sup>, Satish C. Singh<sup>1</sup>, and J. Pablo Canales<sup>3</sup>

3        <sup>1</sup> Institut de Physique du Globe de Paris, Université Paris Cité, 1 Rue Jussieu, 75005 Paris,  
4        France.

5        <sup>2</sup> Presently at School of Ocean and Earth Science, University of Southampton, European Way,  
6        SO14 3ZH Southampton, UK.

7        <sup>3</sup> Department of Geology and Geophysics, Woods Hole Oceanographic Institution, Woods  
8        Hole MA 02543, USA.

9  
10  
11        **Abstract**

12        Oceanic crust at fast-spreading ridges is formed by melt percolating through the Mohorovičić  
13        Transition Zone (MTZ), the boundary between crust and mantle. However, the relationship  
14        between the crustal structures and MTZ remains elusive. Applying full waveform inversion to  
15        wide-angle seismic data acquired near the 9°N East Pacific Rise, we show that the variations  
16        in crustal MTZ thicknesses are inversely correlated along the segment, although their total  
17        cumulative thickness shows little variations. These variations could be attributed to different  
18        melt migration efficiency through MTZ or variation in mantle thermal structures. Thin MTZ  
19        could be due to rapid percolation of melt from mantle to crust whereas the thick MTZ results  
20        from the crystallization of melt within the transition zone. On the other hand, for relatively hot  
21        segments, melt will accumulate at shallower depth within the lower crust. In contrast, melt  
22        could freeze at Moho depth for relatively cold segments thickening the MTZ.

23  
24  
25

## 26 **Plain Language Summary**

27 At the spreading centres where two plates move apart, the basaltic melt produced by  
28 decompression melting of the upwelling mantle forms new oceanic crust. The oceanic crust is  
29 separated from the underlying mantle by the Mohorovičić Transition Zone (MTZ). However,  
30 the relationship between the crustal structures and MTZ is poorly known. We applied seismic  
31 full waveform inversion, a state-of-the-art seismic imaging method, to the wide-angle seismic  
32 data collected from a young oceanic crust near the 9°N East Pacific Rise. We found that the  
33 crustal thickness varies from 5.1 to 6.5 km along a 70 km-long crustal segment. Interestingly,  
34 the MTZ thickness varies between 1.1 to 2.4 km along the segment and is inversely correlated  
35 with crustal thickness. The total cumulative thickness of crust and MTZ keeps almost constant  
36 along the profile. These variations could be explained either by different melt migration  
37 efficiency through MTZ or by changes in mantle thermal structures along the ridge segment.

38

### 39 **Key points:**

- 40 • We apply elastic-wave full waveform inversion to wide-angle seismic data acquired  
41 near the 9°N East Pacific Rise
- 42 • The high-resolution crustal velocity model shows that the crustal thickness varies  
43 between 5.1 and 6.5 km along a 70 km-long crustal segment
- 44 • The thickness of Moho transition zone is inversely correlated with crustal thickness  
45 along the segment

46

47

48

49

50

## 51 **1. Introduction**

52 Oceanic crust is formed at mid-ocean ridges (MORs) from basaltic melt derived from  
53 decompression of upwelling mantle as two lithospheric plates move apart (Cann, 1970). In a  
54 fast and intermediate-spreading environment, the melt rises towards the surface and  
55 accumulates within an axial magma chamber (AMC) at mid-crustal depths (Detrick *et al.*, 1987;  
56 Mutter *et al.*, 1988). A portion of the accumulated melt erupts to form lava flows on the seafloor  
57 and dike underneath, making up the upper crust. The remainder of the melt crystallises within  
58 the AMC, forming the gabbroic lower crust. The crust is separated from the underlying mantle  
59 by the Moho Transition Zone (MTZ). Determining the relationship between the oceanic crustal  
60 structure and the MTZ is critical for understanding the crustal accretion at MORs.

61

62 Traveltime tomography of wide-angle seismic refraction data has revealed that the magmatic  
63 crust consists of two layers: an upper crust characterised by low P-wave velocities ( $V_p$ : 3.0-  
64 6.5 km/s) but high velocity gradients and a lower crust exhibiting high  $V_p$  (6.5-7.1 km/s) and  
65 significantly reduced velocity gradient (Christeson *et al.*, 2019; White *et al.*, 1992). The mantle  
66 underneath has a  $V_p > 7.7$  km/s and consists primarily of peridotite (Christeson *et al.*, 2019;  
67 Wang and Singh, 2022). However, traveltime tomography constrains the lower crustal velocity  
68 using wide-angle reflections (PmP) from the Moho, resulting in a trade-off between the lower  
69 crustal velocity and the Moho depth (Vaddineni *et al.*, 2021). Furthermore, the Moho is  
70 commonly assumed to be a sharp interface in traveltime tomography (Canales *et al.*, 2003;  
71 Vaddineni *et al.*, 2021; Wang and Singh, 2022), which has precluded determining the  
72 relationship between the crustal structure and the MTZ.

73

74 Multi-channel seismic (MCS) data provide reflection images of the oceanic Moho formed at  
75 fast- and intermediate-spreading ridges with seismic characters ranging from impulsive,

76 shingled and diffusive (Aghaei *et al.*, 2014; Kent *et al.*, 1994). The impulsive and shingled  
77 Moho are characterized by a single-phase reflection while the diffusive Moho shows sub-  
78 horizontally multi-phase reflection events (Aghaei *et al.*, 2014; Barth and Mutter, 1996; Kent  
79 *et al.*, 1994). Seismic waveform modelling demonstrates that the impulsive and shingled Moho  
80 reflections are probably produced by a thin MTZ and the diffusive Moho indicates a relatively  
81 thick MTZ (Brocher *et al.*, 1985; Collins *et al.*, 1986). Nedimović *et al.* (2005) suggest that the  
82 multi-phase Moho reflection events might be caused by the frozen magma lenses within a thick  
83 MTZ. However, MCS data provide the Moho structure in two-way traveltimes, which needs to  
84 be converted to depth. Due to the lack of accurate velocity model of the subsurface, the  
85 uncertainty in the inferred Moho depth can be hundreds metres (Aghaei *et al.*, 2014; Barth and  
86 Mutter, 1996), and even >1 km in some cases (Barth and Mutter, 1996). Therefore, our  
87 understanding of MTZ from seismic methods remain elusive.

88

89 Structural mapping of ophiolites, which are thought to be formed at ancient spreading ridges,  
90 indicates that the MTZ is primarily composed of dunites with gabbroic sills and lenses, marking  
91 a gradually downward change from layered gabbro in the lower crust to ultramafic mantle  
92 consisting dominantly of harzburgites (Benn *et al.*, 1988; Boudier and Nicolas, 1995; Karson  
93 *et al.*, 1984). The thickness of the MTZ varies from 5-10 m to 1-3 km (Benn *et al.*, 1988;  
94 Karson *et al.*, 1984), where the thickness of gabbroic sills and lenses can reach hundreds of  
95 meters in a thick MTZ (Benn *et al.*, 1988; Boudier and Nicolas, 1995; Karson *et al.*, 1984). The  
96 strong magmatic flow structures within the MTZ indicate that these gabbroic sills were  
97 emplaced at the ridge axis, implying that a large amount of melt was trapped within the MTZ  
98 during crustal accretion (Boudier and Nicolas, 1995). However, in the absence of drilling  
99 results, we do not have any in situ information about the MTZ.

100

101 Here, we present results of the application of two-dimensional (2-D) elastic full waveform  
102 inversion (FWI) (Shipp and Singh, 2002) to wide-angle seismic data to constrain the  $V_p$  of the  
103 crust and MTZ of young oceanic crust near the East Pacific Rise (EPR) at  $9^{\circ}$ - $10^{\circ}$ N. FWI can  
104 provide high-resolution velocity model of the subsurface at a vertical resolution of half a  
105 wavelength (Virieux and Operto, 2009), i.e. hundreds meter (Guo *et al.*, 2022; Jian *et al.*, 2021),  
106 important for studying the fine-scale structures of oceanic crust and MTZ.

107

## 108 **2. Seismic data and full waveform inversion**

109 The seismic data were acquired from the fast-spreading (11 cm/yr) EPR between  $8^{\circ}15'$ N and  
110  $10^{\circ}05'$ N during the 1997 Undershoot Seismic Experiment (Toomey *et al.*, 1997). Although the  
111 undershoot experiment was performed covering the whole  $9^{\circ}$ N EPR segment on both flanks  
112 (Toomey *et al.*, 1997), here we use only six ocean bottom instruments deployed at dominantly  
113  $\sim$ 8-14 km intervals along a 92 km-long profile on the eastern flank of the EPR (Figure 1)  
114 between the Clipperton transform fault (TF; first-order discontinuity) and the  $9^{\circ}03'$ N  
115 overlapping spreading centre (OSC; second-order discontinuity). The EPR between the  $9^{\circ}03'$ N  
116 OSC and the Clipperton TF is further offset by the third-order discontinuities at  $9^{\circ}12'$ N,  $9^{\circ}20'$ N,  
117  $9^{\circ}37'$ N,  $9^{\circ}51.5'$ N and  $9^{\circ}58'$ N, respectively (black rectangles in Figure 1; (Aghaei *et al.*, 2014;  
118 White *et al.*, 2006)). The source was an airgun array with a total volume of  $8503 \text{ m}^3$ , towed at  
119 10 m depth and fired at  $\sim$  460 m interval.

120

121 We simultaneously inverted the pressure data recorded by ocean bottom hydrophones (OBHs)  
122 and the vertical component data of ocean bottom seismometers (OBSs). We band-pass filtered  
123 the data between 3 and 30 Hz and applied a predictive gapped deconvolution with minimum  
124 and maximum lags of 0.14 s and 0.35 s to suppress the seismic bubbles (Figure S1). The  
125 deconvolved data were transformed from three-dimensional (3-D) to 2-D by multiplying the

126 amplitude of the data by  $\sqrt{t}$  (where  $t$  is the traveltime) and convolving the seismic data with  
127  $1/\sqrt{t}$  (Pica *et al.*, 1990). A 1.0 s-wide time windowing was applied to extract the Pg, PmP and  
128 mantle refraction (Pn) arrivals between 6 and 60 km offsets (Figure S2). The top of the time  
129 window is 0.1 s prior the picked first arrival traveltime. In this work, we inverted the seismic  
130 data of two frequency bands, first 3-5 Hz and then 3-10 Hz. The synthetic seismic data were  
131 modelled by solving the 2-D elastic-wave equation using a time-domain staggered-grid finite-  
132 difference scheme (Levander, 1988) (Text S1). The source wavelets used in synthetic modelling  
133 were estimated by stacking the aligned near-offset water arrivals (Text S2 and Figures S3 and  
134 S4).

135

136 FWI of PmP arrivals is highly nonlinear (Guo *et al.*, 2020) and requires a good initial model  
137 and a misfit function that can correctly model the non-linear part of the critically reflected PmP  
138 arrivals and also can handle the triplication between Pg, PmP and Pn arrivals around critical  
139 angles. We built an initial Vp model (Text S3 and Figure S5) using the tomographic velocity  
140 from Canales *et al.* (2003). Comparisons of observed waveforms and the waveform modelled  
141 using the initial model show no cycle-skipping in the first stage of FWI, indicating the initial  
142 model is close enough to the real velocity of the subsurface. Our FWI workflow was  
143 implemented in two stages (Text S4). In the first stage, we applied a trace normalized FWI (Tao  
144 *et al.*, 2017) to primarily fit the seismic traveltime (or phase) information, which allows to  
145 decouple the complex waveforms associated with the critically reflected PmP arrivals and the  
146 triplication and helps to recover the velocity of the MTZ. The result of trace normalized FWI  
147 was then used as a starting model for the true amplitude FWI in the second stage. The true  
148 amplitude FWI further improves the velocity model as it tries to fit both seismic amplitude and  
149 phase information.

150

151 The synthetic data after FWI match the observed data very well as compared to those modelled  
152 using the tomographic model (Figure 2 and Figure S6). Compared with the starting model  
153 (Figure S5A), the velocity model from FWI (Figure 3A) shows fine-scale structures in the crust.  
154 We conducted checkerboard tests (Text S5 and Figure S7-S10) to assess the resolution of the  
155 FWI result using the same source and receiver geometry as the real data inversion. The  
156 checkerboard tests suggest that the FWI can resolve minimum structures of  $0.3 \times 8$  km size  
157 (vertical  $\times$  horizontal) with 5% velocity anomaly between 10 and 80 km horizontal distance.  
158 We also performed synthetic tests (Text S6) to assess the resolvability of the FWI method for  
159 a thick or thin MTZ. These synthetic tests indicate that the FWI can recover a MTZ as thin as  
160 0.5 km or as thick as 3.5 km between 10 and 80 km horizontal distance (Figure S11-S17).  
161 Therefore, we only interpret the velocity structures between 10 and 80 km horizontal distance.

162

### 163 **3. Results**

#### 164 **Crustal structure**

165 The upper crust is characterized by low  $V_p$  but high vertical velocity gradients (Figures 3A,B,D  
166 and E), where the  $V_p$  increases rapidly from  $3.0 \pm 0.1$  km/s at the basement to  $6.5$  km/s at  $1.8 \pm 0.2$   
167 km depth. However, the inverted velocity model reveals a heterogeneous lower crust, where  
168 alternate high-and-low-velocity layers are observed (Figures 3A,D and E). We used the contour  
169 of vertical velocity gradient of  $0 \text{ s}^{-1}$  to represent the boundaries between the high- and low-  
170 velocity layers (Figure 3B). The thickness of these layers varies from 300-400 m to  $\sim 1$  km. The  
171 maximum velocity reduction within the low-velocity layers is  $\sim 500$  m/s.

172

173 At the base of the model at 8.0-9.5 km depth, a positive high velocity gradient zone is observed  
174 (Figure 3B), separating the typical lower crustal velocity above with the mantle velocity below.

175 We picked the depth of the top of this zone, marked by a vertical velocity gradient of  $0 \text{ s}^{-1}$ , and

176 smoothed it over a horizontal distance of 8 km, which is interpreted as the base of the crust (red  
177 dashed curves in [Figures 3A,B](#)). This base of the crust shallows from a depth of  $\sim 9.5$  km  
178 between 10 and 20 km distance to  $\sim 8.0$  km between 45 and 55 km distance, and it lies between  
179 8.2 and 8.5 km depth further north ([Figure 3B](#)). The mean velocity at the base of the crust is  
180  $\sim 7.0 \pm 0.2$  km/s, consistent with the global average velocity ( $7.1 \pm 0.1$  km/s) at the base of crust  
181 formed at fast-spreading ridges (Christeson *et al.*, 2019).

182

183 The interpreted crustal base derived from the FWI is shallower than the tomographic Moho  
184 from Canales *et al.* (2003) along the entire profile ([Figure 3A](#)). The crustal thickness varies  
185 between 5.1 and 6.5 km (red curve in [Figure 3C](#)) with an average thickness of  $\sim 5.6$  km, thinner  
186 than the average crustal thickness ( $\sim 6.8$  km) obtained from the traveltime tomography (Canales  
187 *et al.*, 2003), but close to that ( $\sim 5.8$  km) estimated from the MCS studies in the neighbouring  
188 region (Aghaei *et al.*, 2014). The crust is thicker south of the 30-40 km horizontal distance at  
189  $\sim 9^{\circ}36'$ - $9^{\circ}41'$ N than to the north, and the thickest crust is observed between 10 and 20 km  
190 horizontal distance at  $\sim 9^{\circ}25'$ - $9^{\circ}30'$ N (red curve in [Figure 3C](#)), which is consistent with the  
191 tomography study (Canales *et al.*, 2003) ([Figure S3B](#)) and seismic reflection study (Aghaei *et*  
192 *al.*, 2014; Barth and Mutter, 1996). The thinnest crust is observed at 40-60 km horizontal  
193 distance at  $9^{\circ}41'$ - $9^{\circ}51'$ N, and the crust gradually thickens by  $\sim 500$  m further north (red curve  
194 in [Figure 3C](#)).

195

### 196 **Moho transition zone (MTZ)**

197 FWI does not provide a sharp boundary for the Moho, but an increase in velocity over a certain  
198 depth range, which we define as the MTZ. The base of the crust with zero velocity gradient  
199 marks the top of the MTZ. We used two approaches to define the bottom of the MTZ: (I) 7.85  
200 km/s velocity contour, the global average velocity at the top of the mantle ( $< 7.5$  Myr) for crust

201 formed at fast-spreading ridges (Christeson *et al.*, 2019) and (II) the base of the high velocity  
202 gradient zone. If we pick the depth of the 7.85 km/s velocity contour (purple dashed curves in  
203 [Figures 3A,B](#)) the thickness of the MTZ would be between 1.1 and 2.4 km (blue dashed curve  
204 in [Figure 3C](#)). If we take the base of the large positive velocity gradient zone as the bottom of  
205 the MTZ (purple solid curves in [Figures 3A,B](#)), the thickness of the MTZ would be between  
206 1.6 and 3.0 km (blue solid curve in [Figure 3C](#)) where the average mantle velocity is  
207  $\sim 7.97 \pm 0.13$  km/s. In both cases, the MTZ is relatively thin south of the 30 km horizontal  
208 distance at 9°36'N (blue curves in [Figure 3C](#)). The thickness of the MTZ shows a negative  
209 correlation with the crustal thickness along the profile, i.e., where the MTZ is thick the crust is  
210 thin, and vice versa ([Figure 3C](#)).

211

#### 212 **4. Discussion and conclusion**

213 Our results show (I) the presence of layered structures in the lower crust, (II) the crust is thin  
214 in the north and thick in the south whereas the MTZ is thick in the north and thin in the south  
215 and (III) there is an inverse correlation between the crustal thickness and the MTZ thickness.

216

217 Seismic reflection studies of the 9°N EPR have shown the presence of axial melt lens (AML)  
218 at 1.4-1.9 km depth in the mid-crust (Detrick *et al.*, 1987; Kent *et al.*, 1993) whereas  
219 tomographic studies indicate the presence of low velocity zone down to 6-7 km depth below  
220 the seafloor (Dunn, 2022; Dunn *et al.*, 2000), indicating the existence of partial melt.  
221 Furthermore, Marjanović *et al.* (2014) and Arnulf *et al.* (2014) show the presence of secondary  
222 melt sills within 1.65 km depth below the AML. Studies of the Oman ophiolite suggest that the  
223 melt can intrude and crystallize at different depths in the lower crust (Boudier *et al.*, 1996;  
224 Kelemen *et al.*, 1997). The observed alternate high-and-low-velocity layering in the lower crust  
225 could be due to melt of different compositions injected and crystallised at different depths

226 within the lower crust (Figure 4). The gabbroic rocks drilled from the Hess Deep in the  
227 equatorial Pacific are mainly composed of olivine, clinopyroxene and plagioclase (Carlson and  
228 Jay Miller, 2004; Lissenberg *et al.*, 2013). A small increase (by 5%) of the olivine content can  
229 lead up to 600 m/s increase in  $V_p$  of the gabbroic rocks (Carlson and Jay Miller, 2004; Guo *et*  
230 *al.*, 2022). Therefore, the low-velocity layers within the lower crust could be formed by melt  
231 with relatively low olivine concentration while the high-velocity layers could represent olivine-  
232 rich gabbroic sills. This interpretation supports the ‘sheeted sill’ model (Boudier *et al.*, 1996;  
233 Kelemen *et al.*, 1997) where in-situ melt intrusion and crystallization form the lower crust.  
234 Moreover, the off-axis melt sills (Aghaei *et al.*, 2017; Canales *et al.*, 2012; Han *et al.*, 2014)  
235 are observed up to a distance of  $\sim 12$  km from the ridge crest and could form gabbroic sills with  
236 different compositions from those formed at the ridge axis, contributing to the formation of a  
237 heterogeneous lower crust.

238

239 An early study using one-dimensional velocity analysis found that the MTZ at  $\sim 9^{\circ}35'N$  EPR  
240 is  $\sim 1.7$  km at 10 km off-axis distance (Vera *et al.*, 1990). Another MCS study from the  
241 intermediate-spreading Juan de Fuca Ridge observed that the MTZ could be up to 2.0 km thick  
242 (Nedimović *et al.*, 2005). These estimates fall in the ranges of MTZ thickness obtained using  
243 FWI, but our results provide a 2-D view continuous over 70 km distance along the profile and  
244 its relationship to crustal structure.

245

246 There are two possibilities for the above observations. The along-strike variations in the MTZ  
247 thickness could be due to the different thermal structures among third-order discontinuities.  
248 Thermal structure plays an important role in controlling the vertical depth of melt introduction  
249 and crystallization at fast-spreading ridges (MacLennan *et al.*, 2004). For a relatively hot ridge  
250 segment, melt will pool and crystallize at shallower depth in the lower crust with little melt

251 accumulate within the MTZ. In contrast, for a relatively cold ridge segment, some melt could  
252 accumulate at deeper depths in the lower crust or at Moho depth, forming a thick MTZ.  
253 Presence of melt around Moho depth beneath the 9-10°N EPR has been observed in the seafloor  
254 compliance (Crawford *et al.*, 1991). The along-strike variations in the MTZ thickness could  
255 also reflect changes in the efficiency of melt migration through the MTZ beneath the spreading  
256 centre. A thin MTZ would indicate a rapid percolation of melt from the upwelling mantle to  
257 the accreting crust. The formation of a thick MTZ could be due to less efficient melt extraction  
258 from mantle to crust leading to the accumulation and crystallization of a large amount of melt  
259 within the transition zone (Figure 4). Melt crystallization might occur in the thin MTZ as well.

260

261 These interpretations are supported by the negative correlation between the thicknesses of the  
262 crust and MTZ. A relatively thick MTZ underlying a relatively thin crust suggests that a  
263 significant part of melt was crystallized in the MTZ. However, the total cumulative thickness  
264 of the crust and MTZ does not vary much along the profile, albeit the total melt supply from  
265 the mantle to crust might be uniform along the entire ridge segment.

266

267 Based on the study of Oman ophiolite, Nicolas *et al.* (1996) found that the thin lower crust is  
268 generally associated with a thick MTZ while the thick lower crust is associated with a thin  
269 MTZ, indicating that there is an anti-correlation between the ophiolite's crustal and MTZ  
270 thicknesses, assuming the combined thickness of the extrusive basalt and sheeted dike is  
271 constant. The extensive presence of thick gabbro sills observed in the relatively thick MTZ in  
272 the Oman ophiolite demonstrate that a large amount of magma has ponded within the MTZ  
273 (Boudier and Nicolas, 1995), supporting our interpretation.

274

275 Along our profile, the change from a relatively thin to thick MTZ occurs over a short distance  
276 of ~10 km (Figure 3C), and a similar pattern has been observed in the Oman ophiolite where  
277 the transition from a thin to thick MTZ occurs over <5 km distance (Jousselin and Nicolas,  
278 2000). The seismic reflection study at 9°N EPR (Aghaei *et al.*, 2014) also found that the  
279 character of the Moho reflection varies over 3-4 km spatial distance. Given different lateral  
280 resolutions of these methods, these observations indicate that the thermal structure and/or melt  
281 migration efficiency through MTZ can vary quickly along the ridge axis at fast-spreading ridge.  
282 Laterally abrupt changes in the thermal structure and melt migration efficiency will influence  
283 ridge segmentation, possibly governing the distributions of third-order ridge discontinuities  
284 (Aghaei *et al.*, 2014).

285

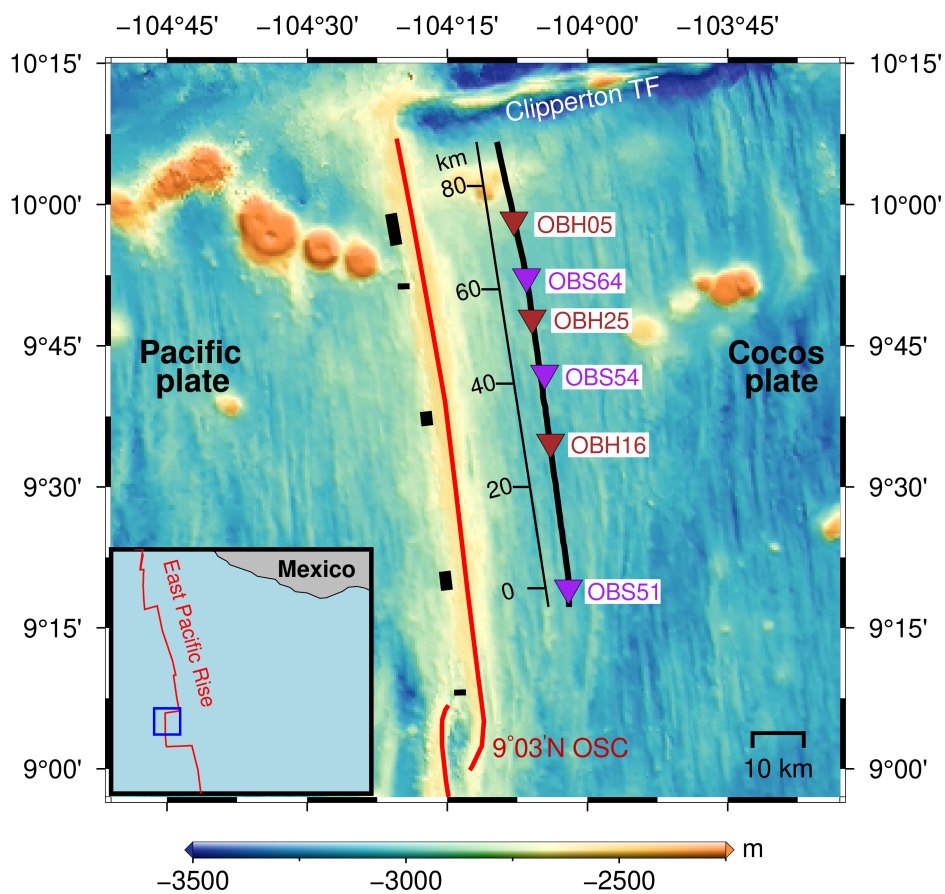
286 The average crustal thickness estimated from MCS data is ~5.8 km in the 9°N EPR region  
287 (Aghaei *et al.*, 2014). However, seismic refraction study in the neighbouring region suggests  
288 ~1 km thicker crust (Canales *et al.*, 2003). This indicates a discrepancy in the oceanic crustal  
289 thickness obtained using seismic refraction and reflection methods, though these study areas  
290 are not exactly the same. The Moho depths estimated from reflection and refraction studies  
291 appear to have good consistency at some regions close to subduction trenches in the Pacific  
292 Ocean (Ivandic *et al.*, 2008; Kodaira *et al.*, 2014). However, in these studies, the Moho depths  
293 estimated from OBS data show large uncertainties of the order of ~1 km. In contrast, FWI of  
294 wide-angle seismic data can provide precise velocity of the crust and upper mantle and  
295 constrain the thickness of the MTZ, reconciling the discrepancy between the seismic reflection  
296 and the refraction methods. Our results demonstrate that the FWI method is a powerful tool for  
297 understanding the structures of crust and MTZ and crustal accretion processes at MORs.

298

299

300 **Figures**

301



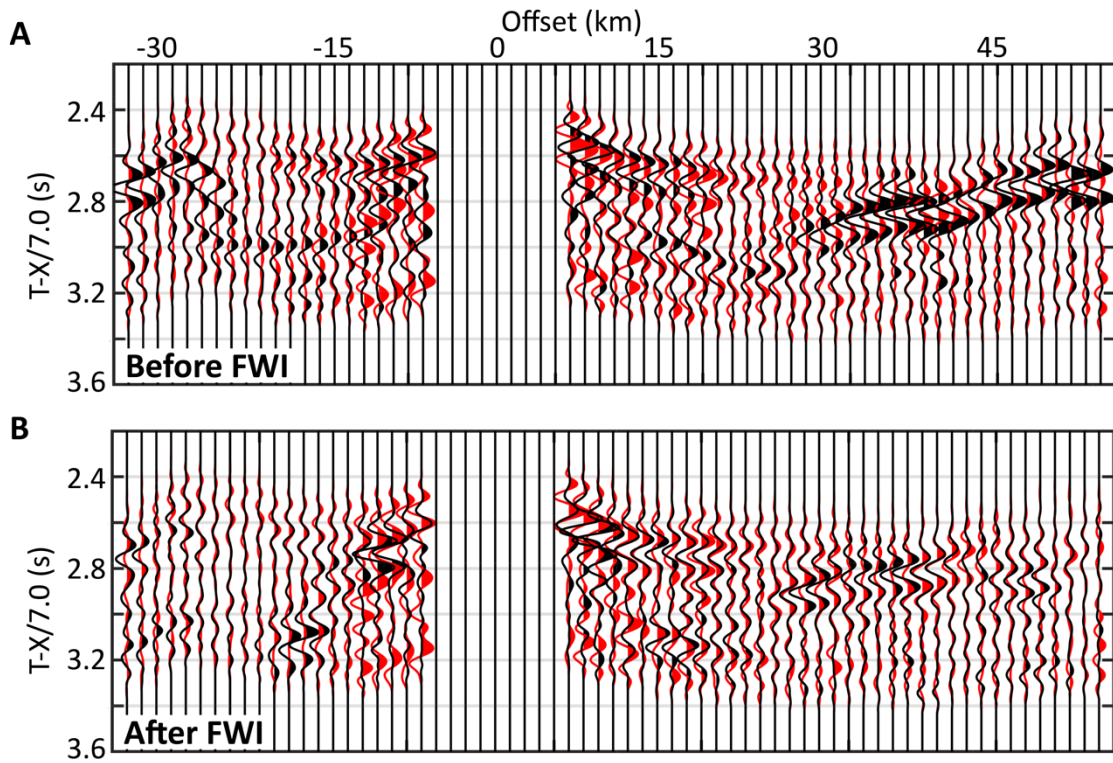
302

303 **Figure 1. Bathymetry map of the study area.** Red curves show the East Pacific Rise between  
304 the Clipperton transform fault (TF) and the 9°03'N overlapping spreading centre (OSC). The  
305 black rectangles show the locations of third-order discontinuities at 9°12'N, 9°20'N, 9°37'N,  
306 9°51.5'N and 9°58'N from south to north, respectively (Aghaei *et al.*, 2014; White *et al.*, 2006).  
307 The black line indicates the seismic profile. Brown and purple triangles represent the locations  
308 of ocean bottom hydrophones (OBHs) and ocean bottom seismometers (OBSs), respectively.  
309 The blue box in the inset shows the location of the study area. The black scale shows the  
310 distance along the profile.

311

312

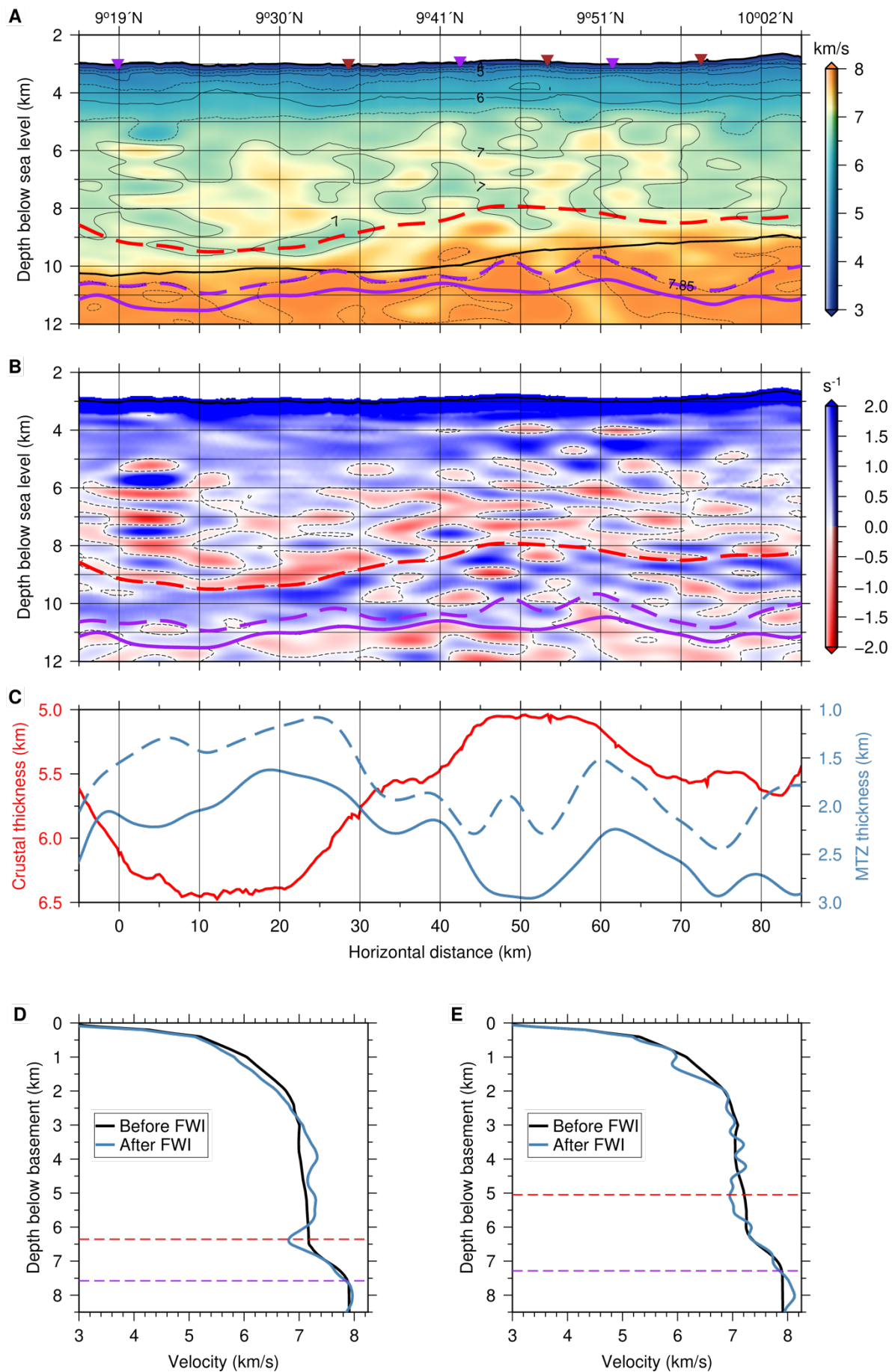
313



315

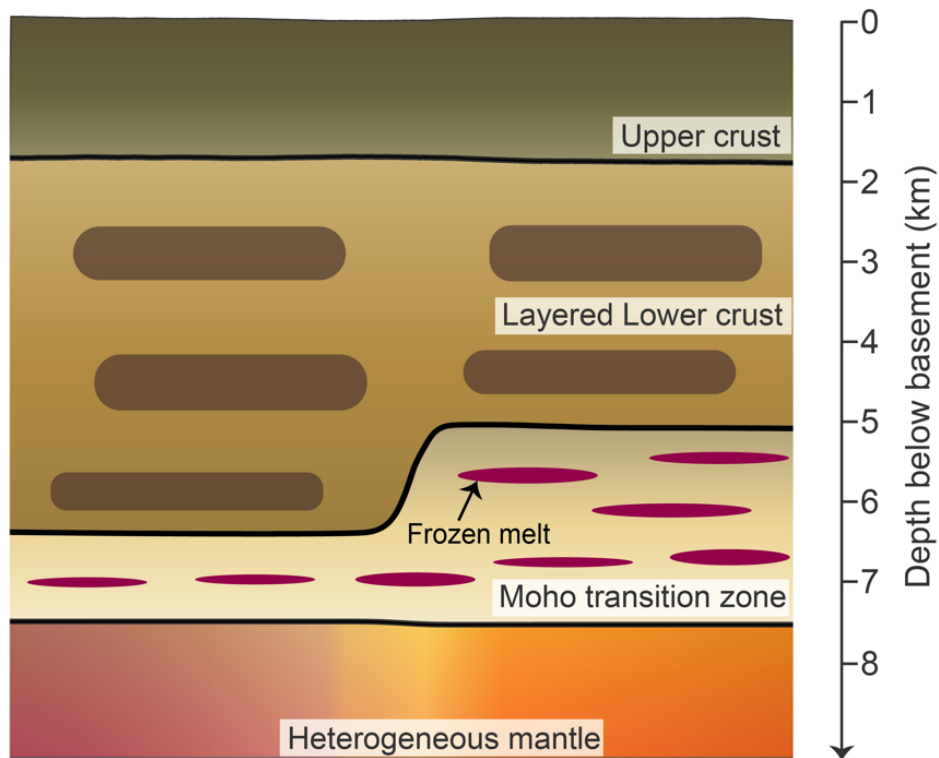
316 **Figure 2. Comparisons of modelled and observed seismic data for OBH25.** (A) Before FWI  
 317 and (B) after FWI. The observed data is filtered to 3-10 Hz and the modelled data are calculated  
 318 using the 3-10 Hz source wavelet. The modelled and observed seismic data are plotted in black  
 319 and red, respectively. Travelttime (T) of the seismic data is reduced using a reduction velocity  
 320 of 7.0 km/s. For better visibility, a scalar weighting factor  $(1 + 0.1 \times X)$  was applied for each  
 321 trace to enhance the amplitude at large offsets, where X is the offset.

322



324 **Figure 3. Results of FWI.** (A) Crustal and upper mantle P-wave velocity model from FWI.  
325 The thick black curve is the tomographic Moho from Canales *et al.* (2003). The red dashed  
326 curve is the interpreted crustal base corresponding to the top of the large positive velocity  
327 gradient zone beneath the crust. The dashed purple curve is the bottom of the MTZ interpreted  
328 using a smooth version of the 7.85 km/s velocity contour (Christeson *et al.*, 2019). The solid  
329 purple curve is the bottom of the MTZ interpreted using the base of the large positive velocity  
330 gradient zone. The 4.5, 5.5, 6.5 and 7.85 km/s velocity contours are shown as black dashed  
331 curves from top to bottom. The brown and purple triangles show the locations of OBHs and  
332 OBSs, respectively. (B) Vertical velocity gradient. The black dashed curves are the  $0 \text{ s}^{-1}$  velocity  
333 gradient contour. The red and the purple curves are the same as in A. (C) The crustal (in red)  
334 and the MTZ thickness (in blue) variations along the profile. The blue dashed and solid curves  
335 are the MTZ thickness calculated using a smooth version of the 7.85 km/s velocity contour  
336 (purple dashed curves in A,B) and using the base of the large positive velocity gradient zone  
337 (purple solid curves in A,B) as the bottom of the MTZ, respectively. (D) Comparison of the  
338 starting (in black) and final (in blue) inverted velocity profiles averaged between 16 and 24 km  
339 horizontal distance where the crust is thick and the MTZ is thin. (E) Comparison of the starting  
340 (in black) and final (in blue) inverted velocity profiles averaged between 46 and 54 km  
341 horizontal distance where the crust is thin and the MTZ is thick. The red and purple dashed  
342 lines in d and e represent the top of the MTZ and the MTZ bottom defined by 7.85 km/s velocity  
343 contour.

344



345

346

347 **Figure 4. Schematic diagram showing structures of the oceanic crust and Moho transition**

348 **zone (MTZ).** The oceanic crust is separated into an upper crust (~1.8 km thick) and a layered

349 lower crust. The dark brown blocks in the lower crust refer to the low-velocity layers from FWI.

350 The layered lower crust indicates the oceanic lower crust is formed by in-situ melt injection

351 and crystallization at different depths. The thickness of the MTZ varies along strike between

352 1.1 and 2.4 km, inversely correlated with the crustal thickness. The red horizontal elongated

353 ellipsoids represent the frozen gabbro sills, which is accumulated and crystallized during its

354 migration from the upwelling mantle to the crust.

355

## 356 REFERENCES

- 357 Aghaei, O., M. R. Nedimović, H. Carton, S. M. Carbotte, J. P. Canales, and J. C. Mutter  
358 (2014), Crustal thickness and Moho character of the fast-spreading East Pacific Rise from 9°  
359 42'N to 9°57'N from poststack-migrated 3-D MCS data, *Geochem. Geophys. Geosyst.*, *15*(3),  
360 634-657, doi:<https://doi.org/10.1002/2013GC005069>.
- 361 Aghaei, O., M. R. Nedimović, M. Marjanović, S. M. Carbotte, J. Pablo Canales, H. Carton,  
362 and N. Nikić (2017), Constraints on melt content of off-axis magma lenses at the East Pacific  
363 Rise from analysis of 3-D seismic amplitude variation with angle of incidence, *J. Geophys.*  
364 *Res.*, *122*(6), 4123-4142, doi:<https://doi.org/10.1002/2016JB013785>.
- 365 Arnulf, A. F., S. C. Singh, and J. W. Pye (2014), Seismic evidence of a complex multi-lens  
366 melt reservoir beneath the 9° N Overlapping Spreading Center at the East Pacific Rise,  
367 *Geophys. Res. Lett.*, *41*(17), 6109-6115, doi:<https://doi.org/10.1002/2014GL060859>.
- 368 Barth, G. A., and J. C. Mutter (1996), Variability in oceanic crustal thickness and structure:  
369 Multichannel seismic reflection results from the northern East Pacific Rise, *J. Geophys. Res.*,  
370 *101*(B8), 17951-17975, doi:<https://doi.org/10.1029/96JB00814>.
- 371 Benn, K., A. Nicolas, and I. Reuber (1988), Mantle—crust transition zone and origin of  
372 wehrlitic magmas: Evidence from the Oman ophiolite, *Tectonophysics*, *151*(1), 75-85,  
373 doi:[https://doi.org/10.1016/0040-1951\(88\)90241-7](https://doi.org/10.1016/0040-1951(88)90241-7).
- 374 Boudier, F., and A. Nicolas (1995), Nature of the Moho Transition Zone in the Oman  
375 Ophiolite, *J. Petrol.*, *36*(3), 777-796, doi:10.1093/petrology/36.3.777.
- 376 Boudier, F., A. Nicolas, and B. Ildefonse (1996), Magma chambers in the Oman ophiolite: fed  
377 from the top and the bottom, *Earth Planet. Sci. Lett.*, *144*(1), 239-250,  
378 doi:[https://doi.org/10.1016/0012-821X\(96\)00167-7](https://doi.org/10.1016/0012-821X(96)00167-7).
- 379 Brocher, T. M., J. A. Karson, and J. A. Collins (1985), Seismic stratigraphy of the oceanic  
380 Moho based on ophiolite models, *Geology*, *13*(1), 62-65, doi:10.1130/0091-  
381 7613(1985)13<62:SSotom>2.0.Co;2.
- 382 Canales, J. P., H. Carton, S. M. Carbotte, J. C. Mutter, M. R. Nedimović, M. Xu, O. Aghaei,  
383 M. Marjanović, and K. Newman (2012), Network of off-axis melt bodies at the East  
384 Pacific Rise, *Nature Geosci.*, *5*(4), 279-283, doi:10.1038/ngeo1377.
- 385 Canales, P. J., R. S. Detrick, D. R. Toomey, and W. S. D. Wilcock (2003), Segment-scale  
386 variations in the crustal structure of 150–300 kyr old fast spreading oceanic crust (East  
387 Pacific Rise, 8°15'N–10°5'N) from wide-angle seismic refraction profiles, *Geophys. J. Int.*,  
388 *152*(3), 766-794, doi:10.1046/j.1365-246X.2003.01885.x.
- 389 Cann, J. R. (1970), New Model for the Structure of the Ocean Crust, *Nature*, *226*(5249), 928-  
390 930, doi:10.1038/226928a0.
- 391 Carlson, R. L., and D. Jay Miller (2004), Influence of pressure and mineralogy on seismic  
392 velocities in oceanic gabbros: Implications for the composition and state of the lower oceanic  
393 crust, *J. Geophys. Res.*, *109*(B9), B09205, doi:<https://doi.org/10.1029/2003JB002699>.
- 394 Christeson, G. L., J. A. Goff, and R. S. Reece (2019), Synthesis of Oceanic Crustal Structure  
395 From Two-Dimensional Seismic Profiles, *Rev. Geophys.*, *57*(2), 504-529,  
396 doi:<https://doi.org/10.1029/2019RG000641>.
- 397 Collins, J. A., T. M. Brocher, and J. A. Karson (1986), Two-dimensional seismic reflection  
398 modeling of the inferred fossil oceanic crust/mantle transition in the Bay of Islands Ophiolite,  
399 *J. Geophys. Res.*, *91*(B12), 12520-12538, doi:<https://doi.org/10.1029/JB091iB12p12520>.
- 400 Crawford, W. C., S. C. Webb, and J. A. Hildebrand (1991), Seafloor compliance observed by  
401 long-period pressure and displacement measurements, *J. Geophys. Res.*, *96*(B10), 16151-  
402 16160, doi:<https://doi.org/10.1029/91JB01577>.

403 Detrick, R. S., P. Buhl, E. Vera, J. Mutter, J. Orcutt, J. Madsen, and T. Brocher (1987), Multi-  
404 channel seismic imaging of a crustal magma chamber along the East Pacific Rise, *Nature*,  
405 326(6108), 35-41, doi:10.1038/326035a0.

406 Dunn, R. A. (2022), A Dual-Level Magmatic System Beneath the East Pacific Rise, 9°N,  
407 *Geophys. Res. Lett.*, 49(18), e2022GL097732, doi:<https://doi.org/10.1029/2022GL097732>.

408 Dunn, R. A., D. R. Toomey, and S. C. Solomon (2000), Three-dimensional seismic structure  
409 and physical properties of the crust and shallow mantle beneath the East Pacific Rise at  
410 9°30'N, *J. Geophys. Res.*, 105(B10), 23537-23555,  
411 doi:<https://doi.org/10.1029/2000JB900210>.

412 Guo, P., S. C. Singh, V. Vaddineni, I. Grevemeyer, and E. Saygin (2022), Lower oceanic crust  
413 formed by in situ melt crystallization revealed by seismic layering, *Nature Geosci.*, 15, 591–  
414 596, doi:<https://doi.org/10.1038/s41561-022-00963-w>.

415 Guo, P., S. C. Singh, V. A. Vaddineni, G. Visser, I. Grevemeyer, and E. Saygin (2020),  
416 Nonlinear full waveform inversion of wide-aperture OBS data for Moho structure using a  
417 trans-dimensional Bayesian method, *Geophys. J. Int.*, 224(2), 1056-1078,  
418 doi:10.1093/gji/ggaa505.

419 Han, S., S. M. Carbotte, H. Carton, J. C. Mutter, O. Aghaei, M. R. Nedimović, and J. P.  
420 Canales (2014), Architecture of on- and off-axis magma bodies at EPR 9°37–40'N and  
421 implications for oceanic crustal accretion, *Earth Planet. Sci. Lett.*, 390, 31-44,  
422 doi:<https://doi.org/10.1016/j.epsl.2013.12.040>.

423 Ivandic, M., I. Grevemeyer, A. Berhorst, E. R. Flueh, and K. McIntosh (2008), Impact of  
424 bending related faulting on the seismic properties of the incoming oceanic plate offshore of  
425 Nicaragua, *J. Geophys. Res.*, 113(B5), doi:<https://doi.org/10.1029/2007JB005291>.

426 Jian, H., M. R. Nedimović, J. P. Canales, and K. W. H. Lau (2021), New Insights Into the Rift  
427 to Drift Transition Across the Northeastern Nova Scotian Margin From Wide-Angle Seismic  
428 Waveform Inversion and Reflection Imaging, *J. Geophys. Res.*, 126(12), e2021JB022201,  
429 doi:<https://doi.org/10.1029/2021JB022201>.

430 Joussetin, D., and A. Nicolas (2000), The Moho transition zone in the Oman ophiolite-  
431 relation with wehrlites in the crust and dunites in the mantle, *Mar. Geophys. Res.*, 21(3), 229-  
432 241, doi:10.1023/A:1026733019682.

433 Karson, J. A., J. A. Collins, and J. F. Casey (1984), Geologic and seismic velocity structure of  
434 the crust/mantle transition in the Bay of Islands Ophiolite Complex, *J. Geophys. Res.*,  
435 89(B7), 6126-6138, doi:<https://doi.org/10.1029/JB089iB07p06126>.

436 Kelemen, P. B., K. Koga, and N. Shimizu (1997), Geochemistry of gabbro sills in the crust-  
437 mantle transition zone of the Oman ophiolite: implications for the origin of the oceanic lower  
438 crust, *Earth Planet. Sci. Lett.*, 146(3), 475-488, doi:[https://doi.org/10.1016/S0012-821X\(96\)00235-X](https://doi.org/10.1016/S0012-821X(96)00235-X).

440 Kent, G. M., A. J. Harding, and J. A. Orcutt (1993), Distribution of magma beneath the East  
441 Pacific Rise between the Clipperton Transform and the 9°17'N Deval from forward modeling  
442 of common depth point data, *J. Geophys. Res.*, 98(B8), 13945-13969,  
443 doi:<https://doi.org/10.1029/93JB00705>.

444 Kent, G. M., A. J. Harding, J. A. Orcutt, R. S. Detrick, J. C. Mutter, and P. Buhl (1994),  
445 Uniform accretion of oceanic crust south of the Garrett transform at 14°15'S on the East  
446 Pacific Rise, *J. Geophys. Res.*, 99(B5), 9097-9116, doi:<https://doi.org/10.1029/93JB02872>.

447 Kodaira, S., G. Fujie, M. Yamashita, T. Sato, T. Takahashi, and N. Takahashi (2014),  
448 Seismological evidence of mantle flow driving plate motions at a palaeo-spreading centre,  
449 *Nature Geosci.*, 7(5), 371-375, doi:10.1038/ngeo2121.

450 Levander, A. R. (1988), Fourth-order finite-difference P-SV seismograms, *Geophysics*,  
451 53(11), 1425-1436, doi:10.1190/1.1442422.

452 Lissenberg, C. J., C. J. MacLeod, K. A. Howard, and M. Godard (2013), Pervasive reactive  
453 melt migration through fast-spreading lower oceanic crust (Hess Deep, equatorial Pacific  
454 Ocean), *Earth Planet. Sci. Lett.*, *361*, 436-447, doi:<https://doi.org/10.1016/j.epsl.2012.11.012>.  
455 Maclennan, J., T. Hulme, and S. C. Singh (2004), Thermal models of oceanic crustal  
456 accretion: Linking geophysical, geological and petrological observations, *Geochem. Geophys.*  
457 *Geosyst.*, *5*(2), doi:<https://doi.org/10.1029/2003GC000605>.  
458 Marjanović, M., S. M. Carbotte, H. Carton, M. R. Nedimović, J. C. Mutter, and J. P. Canales  
459 (2014), A multi-sill magma plumbing system beneath the axis of the East Pacific Rise, *Nature*  
460 *Geosci.*, *7*(11), 825-829, doi:10.1038/ngeo2272.  
461 Mutter, J. C., G. A. Barth, P. Buhl, R. S. Detrick, J. Orcutt, and A. Harding (1988), Magma  
462 distribution across ridge-axis discontinuities on the East Pacific Rise from multichannel  
463 seismic images, *Nature*, *336*(6195), 156-158, doi:10.1038/336156a0.  
464 Nedimović, M. R., S. M. Carbotte, A. J. Harding, R. S. Detrick, J. P. Canales, J. B. Diebold,  
465 G. M. Kent, M. Tischer, and J. M. Babcock (2005), Frozen magma lenses below the oceanic  
466 crust, *Nature*, *436*(7054), 1149-1152, doi:10.1038/nature03944.  
467 Nicolas, A., F. Boudier, and B. Ildefonse (1996), Variable crustal thickness in the Oman  
468 ophiolite: Implication for oceanic crust, *J. Geophys. Res.*, *101*(B8), 17941-17950,  
469 doi:<https://doi.org/10.1029/96JB00195>.  
470 Pica, A., J. P. Diet, and A. Tarantola (1990), Nonlinear inversion of seismic reflection data in  
471 a laterally invariant medium, *Geophysics*, *55*(3), 284-292, doi:10.1190/1.1442836.  
472 Shipp, R. M., and S. C. Singh (2002), Two-dimensional full wavefield inversion of wide-  
473 aperture marine seismic streamer data, *Geophys. J. Int.*, *151*(2), 325-344, doi:10.1046/j.1365-  
474 246X.2002.01645.x.  
475 Tao, K., S. P. Grand, and F. Niu (2017), Full-waveform inversion of triplicated data using a  
476 normalized-correlation-coefficient-based misfit function, *Geophys. J. Int.*, *210*(3), 1517-1524,  
477 doi:10.1093/gji/ggx249.  
478 Toomey, D. R., R. S. Detrick, and W. S. D. Wilcock (1997), Mapping melt and matrix flow in  
479 the uppermost mantle: undershooting the East Pacific Rise between the Siqueiros and  
480 Clipperton, R/V Maurice Ewing Leg 97-08, *Cruise Report, p. 163, Woods Hole Oceanogr.*  
481 *Inst., Woods Hole, MA*.  
482 Vaddineni, V. A., S. C. Singh, I. Grevemeyer, P. Audhkhasi, and C. Papenberg (2021),  
483 Evolution of the Crustal and Upper Mantle Seismic Structure From 0-27 Ma in the  
484 Equatorial Atlantic Ocean at 2° 43'S, *J. Geophys. Res.*, *126*(6), e2020JB021390,  
485 doi:<https://doi.org/10.1029/2020JB021390>.  
486 Vera, E. E., J. C. Mutter, P. Buhl, J. A. Orcutt, A. J. Harding, M. E. Kappus, R. S. Detrick, and  
487 T. M. Brocher (1990), The structure of 0- to 0.2-m.y.-old oceanic crust at 9°N on the East  
488 Pacific Rise from expanded spread profiles, *J. Geophys. Res.*, *95*(B10), 15529-15556,  
489 doi:10.1029/JB095iB10p15529.  
490 Virieux, J., and S. Operto (2009), An overview of full waveform inversion in exploration  
491 geophysics, *Geophysics*, *74*(6), WCC1-WCC26, doi:<https://doi.org/10.1190/1.3238367>.  
492 Wang, Z., and S. C. Singh (2022), Seismic evidence for uniform crustal accretion along slow-  
493 spreading ridges in the equatorial Atlantic Ocean, *Nat. Commun.*, *13*(1), 7809,  
494 doi:10.1038/s41467-022-35459-z.  
495 Wang, Z., S. C. Singh, and J. P. Canales (2024), Wide-angle seismic refraction data from the  
496 northern portion of the outer eastern profile, 9°N East Pacific Rise, *IPGP Research*  
497 *Collection*, url:[https://dataverse.ipgp.fr/privateurl.xhtml?token=6eca5518-ffd6-4737-a016-  
498 32f5d28f5fea](https://dataverse.ipgp.fr/privateurl.xhtml?token=6eca5518-ffd6-4737-a016-32f5d28f5fea).  
499 White, R. S., D. McKenzie, and R. K. O'Nions (1992), Oceanic crustal thickness from  
500 seismic measurements and rare earth element inversions, *J. Geophys. Res.*, *97*(B13), 19683-  
501 19715, doi:<https://doi.org/10.1029/92JB01749>.

502 White, S. M., R. M. Haymon, and S. Carbotte (2006), A new view of ridge segmentation and  
503 near-axis volcanism at the East Pacific Rise, 8°–12°N, from EM300 multibeam bathymetry,  
504 *Geochem. Geophys. Geosyst.*, 7(12), doi:<https://doi.org/10.1029/2006GC001407>.  
505

506

507

## 508 **Acknowledgements**

509 We thank the captain, crew and scientific team of the R/V Maurice Ewing Leg 97-08 for the  
510 data collection. Acquisition of the data used in this study was supported by NSF Award OCE-  
511 9634132. Z. Wang's contributions to this work were supported by the postdoctoral fellowship  
512 from the GPX project of Institut de Physique du Globe de Paris and partially by the Newton  
513 International Fellowships from the Royal Society. J.P. Canales' contributions to this study were  
514 supported by NSF Award OCE-0118383 and by the Independent Research & Development  
515 Program at WHOI. Results presented in this paper were performed either on the S-CAPAD  
516 platform of Institut de Physique du Globe de Paris or on the IRIDIS High Performance  
517 Computing Facility of the University of Southampton, and we acknowledge the associated  
518 support services in the completion of this work.

519

## 520 **Author Contributions**

521 Z.W. processed the data and wrote the paper. S.C.S. developed the project, supervised the data  
522 processing and wrote the paper. J.P.C. provided the tomographic velocity model. All authors  
523 discussed the results, participated in interpretation, and contributed to paper writing.

524

## 525 **Competing Interests**

526 The authors declare that they have no competing interests.

527

## 528 **Open Research**

529 The seismic data used in this study are available at the Institut de Physique du Globe de Paris  
530 (IPGP) Research Collection (Wang *et al.*, 2024).